Supporting Information for "Episodic Subglacial Drainage Outbursts Below the Northeast Greenland Ice Stream"

J. K. Andersen[1], N. Rathmann[2], C. S. Hvidberg[2], A. Grinsted[2], A. Kusk[1], J. P. Merryman Boncori[1], and J. Mouginot[3]

[1]DTU Space, Tech. Univ. of Denmark, 2800 Kgs. Lyngby, Denmark

[2]Niels Bohr Institute, Univ. of Copenhagen, 2100 Copenhagen, Denmark

[3]Univ. Grenoble Alpes, CNRS, IRD, Grenoble INP, IGE, 38000 Grenoble, France

Contents of this file

1. Text S1 to S2

2. Figures S1 to S9

Additional Supporting Information (Files uploaded separately)

1. Caption for Movie S1

Corresponding author: J. K. Andersen, DTU Space, Tech. Univ. of Denmark, 2800 Kgs. Lyngby, Denmark (jkvand@space.dtu.dk)

Introduction This Supporting Information document contains two additional methodology sections (Text S1 and S2), which elaborate on the data processing steps carried out, and nine figures, which provide support for the applied methodology (Figures S1-S3) and the analysis and discussion of results presented in the manuscript (Figures S4-S9). Additionally, the document contains a caption for the supplementary Movie S1.

Text S1. Sentinel-1 DInSAR measurements Sentinel-1 interferograms were processed using the approach outlined in (Andersen et al., 2020; Kusk et al., 2022). For coregistering images, a 2016-2019 multi-year average velocity map generated by PROMICE (Solgaard et al., 2021) and the TanDEM-X Digital Elevation Model (Rizzoli et al., 2017) were used. The latter was also used for topographic phase flattening. Interferograms are multi-looked with a factor of 15 x 3 in range/azimuth and unwrapped using a Minimum Cost Flow algorithm. Calibration is performed using Ground Control Points in slow-moving regions (velocity magnitude below 35 m/y) where LoS velocities are assumed equal to those derived from the 2016-2019 PROMICE average map. The output 6-day LoS velocity maps were resampled to 50 m x 50 m grids (one for each processed Sentinel-1 track). The DTU IPP software (Kusk et al., 2018) was used for all interferometric processing.

Text S2. Drainage propagation pathways based on hydro-potential As described in the main text section 3.3, we compare the subglacial drainage propagation pathways inferred from DInSAR measurements with those expected from following the negative hydro-potential gradient. We compute hydro-potential (also known as hydraulic potential) under the assumption that the subglacial water pressure is equal to ice overburden pressure (Shreve, 1972):

$$\phi_h = \rho_i g S + [\rho_w - \rho_i]\, g z \tag{1}$$

where ρ_i and ρ_w are the densities of ice and water (taken as 917 kg/m^3 and 1000 kg/m^3, respectively), g is the gravitational acceleration (taken as 9.8 m/s^2), S is the ice surface elevation and z is the bed elevation (both taken from BedMachine v4). Note that this computation neglects the presence of a firn layer. We use the TopoToolbox (Schwanghart & Scherler, 2014) in MATLAB to generate a flow accumulation map, which illustrates expected preferential pathways for subglacial water flow. In order to do this, the local water flow direction is inferred as the steepest negative hydro-potential gradient (using the *FLOWobj* function in TopoToolbox). Prior to this step, hydro-potential sinks have been filled (using the *fillsinks* function). The flow accumulation map is then generated through the *flowacc* function, which outputs, on a pixel level, the number of upgradient grid cells that are drained through the given pixel. In illustrating the hydro-potential-based flow pathways (Fig. 1b in the main text), we threshold the flow accumulation map with a threshold of 75 grid cells/pixels. In Figure 1b, all pixels with a flow accumulation of more than 75 grid cells are shown by the same color (black).

Movie S1. Time series showing vertical displacement anomaly maps, inferred from Sentinel-1 DInSAR LoS velocity anomaly measurements (all from descending track 112), covering parts of the upstream Northeast Greenland Ice Stream region (blue rectangle in Figure 1 of the main text) for 6-day intervals during January to December 2020. Localized uplift events (i.e. positive values, shown in red) are observed to propagate downstream, separating in two branches in July. The uplift is generally followed by subsidence (i.e.

negative values, shown in blue) of a smaller magnitude for several weeks following the initial uplift event.

References

Andersen, J. K., Kusk, A., Boncori, J. P. M., Hvidberg, C. S., & Grinsted, A. (2020). Improved Ice Velocity Measurements with Sentinel-1 TOPS Interferometry. *Remote Sensing*, *12*(12), 2014. doi: 10.3390/rs12122014

Kusk, A., Andersen, J. K., & Boncori, J. P. M. (2022). Burst Overlap Coregistration for Sentinel-1 TOPS DInSAR Ice Velocity Measurements. *IEEE Geoscience and Remote Sensing Letters*, *19*, 1–5. doi: 10.1109/LGRS.2021.3062905

Kusk, A., Boncori, J. M., & Dall, J. (2018). An automated system for ice velocity measurement from SAR. In *EUSAR 2018 12th European Conference on Synthetic Aperture Radar*. Frankfurt am Main: VDE IEEE.

Rizzoli, P., Martone, M., Gonzalez, C., Wecklich, C., Borla Tridon, D., Bräutigam, B., ... Moreira, A. (2017, October). Generation and performance assessment of the global TanDEM-X digital elevation model. *ISPRS Journal of Photogrammetry and Remote Sensing*, *132*, 119–139. doi: 10.1016/j.isprsjprs.2017.08.008

Schwanghart, W., & Scherler, D. (2014). Short Communication: TopoToolbox 2 – MATLAB-based software for topographic analysis and modeling in Earth surface sciences. *Earth Surface Dynamics*, *2*(1), 1–7. doi: 10.5194/esurf-2-1-2014

Shreve, R. L. (1972). Movement of Water in Glaciers. *Journal of Glaciology*, *11*(62), 205–214. doi: 10.1017/S002214300002219X

Solgaard, A., Kusk, A., Merryman Boncori, J. P., Dall, J., Mankoff, K. D., Ahlstrøm,

A. P., . . . Fausto, R. S. (2021). Greenland ice velocity maps from the promice project.

Earth System Science Data, *13*(7), 3491–3512. doi: 10.5194/essd-13-3491-2021

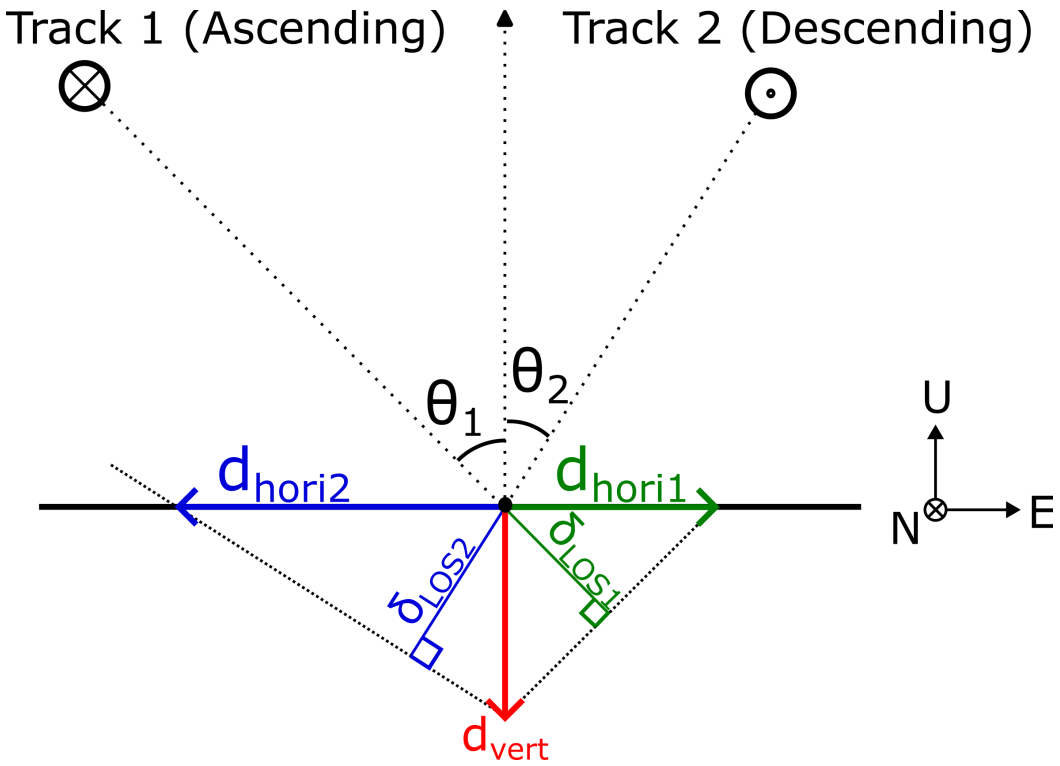

Figure S1. Sketch showing the SAR acquisition geometry of one ascending (i.e. satellite is traveling roughly from South to North) and one descending (i.e. satellite traveling roughly from North to South) satellite track in a local East-North-Up coordinate system. The dotted lines indicate the line-of-sight (LoS) from the satellite to the observed point on ground (black dot). Note that the Sentinel-1 satellites are permanently right-looking. Incidence angles are indicated by θ (for Sentinel-1, values are in the interval 30-45°). The sketch demonstrates how a vertical displacement, d_{vert} (in this case subsidence), would contribute a LoS signal of the same sign in the ascending and descending retrievals. Conversely, horizontal motion, for instance in the East direction, would yield contributions of opposite signs in the ascending and descending LoS motion retrievals.

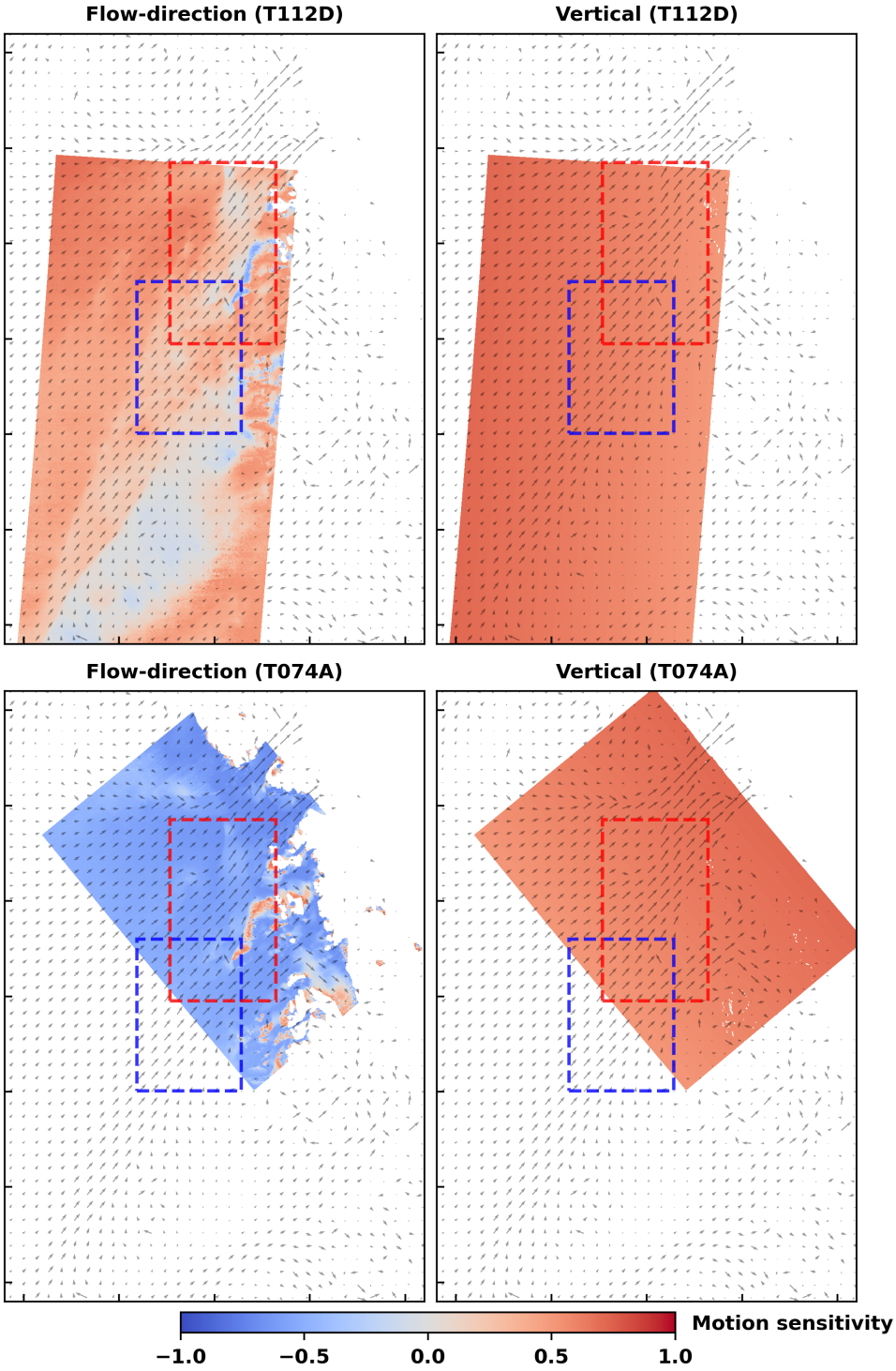

Figure S2. (Caption on next page).

Figure S2. (Previous page) Plots showing the sensitivity of Sentinel-1 DInSAR measurements to motion along the time averaged flow-direction (left column) and the vertical (right column). The top row shows sensitivities for the descending track 112, while the bottom row shows sensitivities for the ascending track 74. Gray quivers indicate the 2016-2019 PROMICE average velocity magnitude map, which was also used to estimate the flow-direction, and the blue and red dashed rectangles indicate the extents of main text Figures 2a and 2b, respectively (also shown in main text Figure 1). Note that for track 112, the two sensitivities are of the same sign (although the sensitivity to horizontal flow-directed motion is relatively lower), while for track 74, the two sensitivities are of comparable magnitudes but opposite signs.

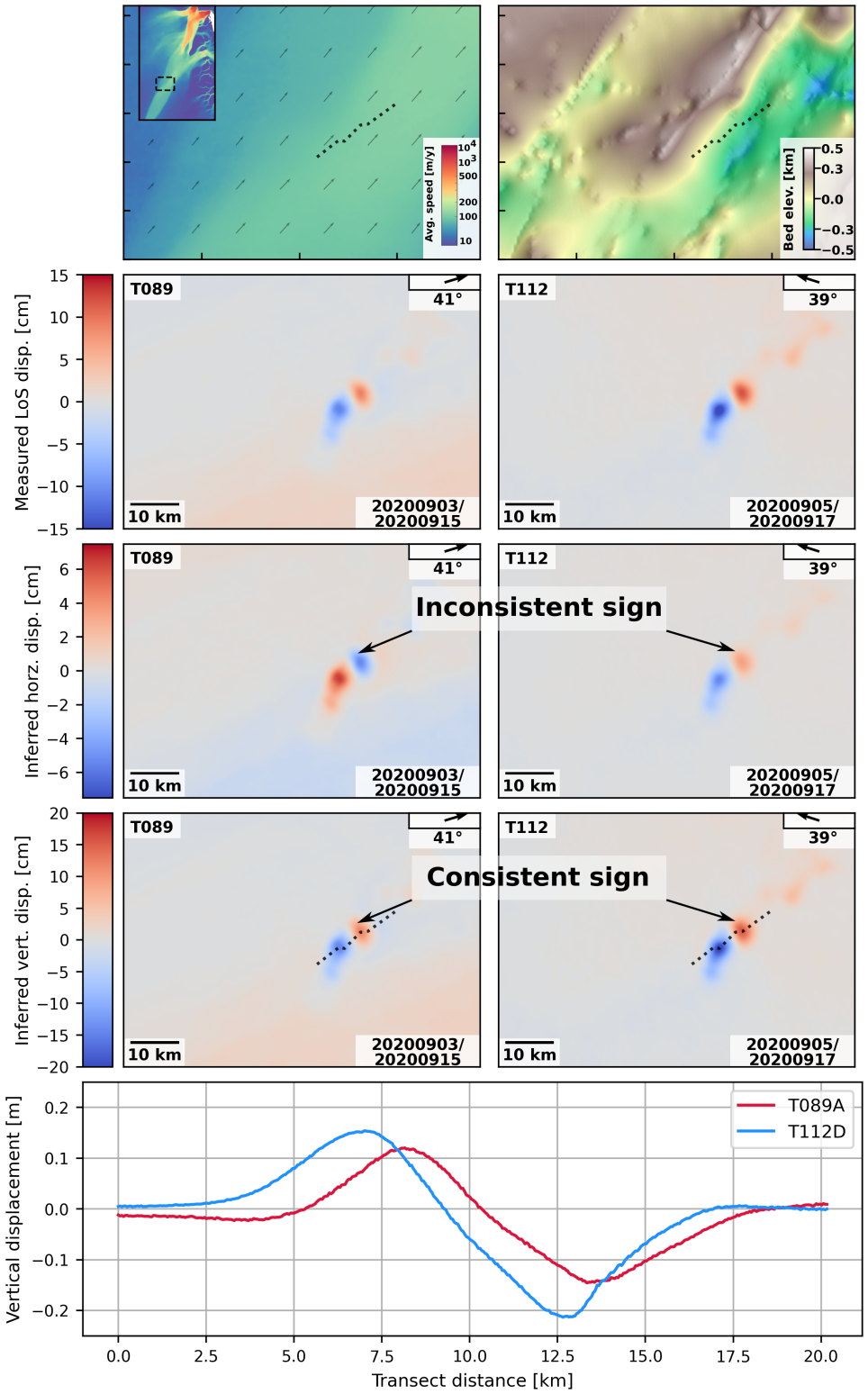

Figure S3. (Caption on next page).

Figure S3. **(Previous page)** (First row) 2016-2019 average ice velocity magnitude (PROMICE) and bed elevation (BedMachine v4) in a small region in upstream NEGIS (see inset in first panel). (Second row) measured line-of-sight (LoS) displacement anomaly (with respect to 2016-2021 median) from the overlapping Sentinel-1 tracks 89 (ascending) and 112 (descending). The ground-projected LoS vector for each track is shown in the top right corner, along with the incidence angle (measured in the center of the region of interest). Note that the features of the LoS anomaly have the same sign in the ascending and descending retrievals. (Third row) Horizontal displacement (in the flow direction estimated from the PROMICE 2016-2019 average velocity product), if the LoS anomalies are assumed to arise purely from a change in flow speed. Note that features are of opposite signs between the ascending and descending retrievals, suggesting that a flow speed change is not consistent with the observations (assuming a constant flow direction). (Fourth row) Inferred vertical displacement, if the LoS anomalies are assumed to arise purely from vertical motion. In this case, the two tracks yield similar results, suggesting that the observations are consistent with the assumption of vertical displacements. (Fifth row) Transect plot showing interpreted vertical displacement from the ascending and descending tracks. Note that both the spatial extent and the magnitude of the uplift/subsidence pattern slightly differ between the two acquisitions, most likely due to the temporal separation between the 12-day baselines of the two retrievals (as well as potential calibration errors).

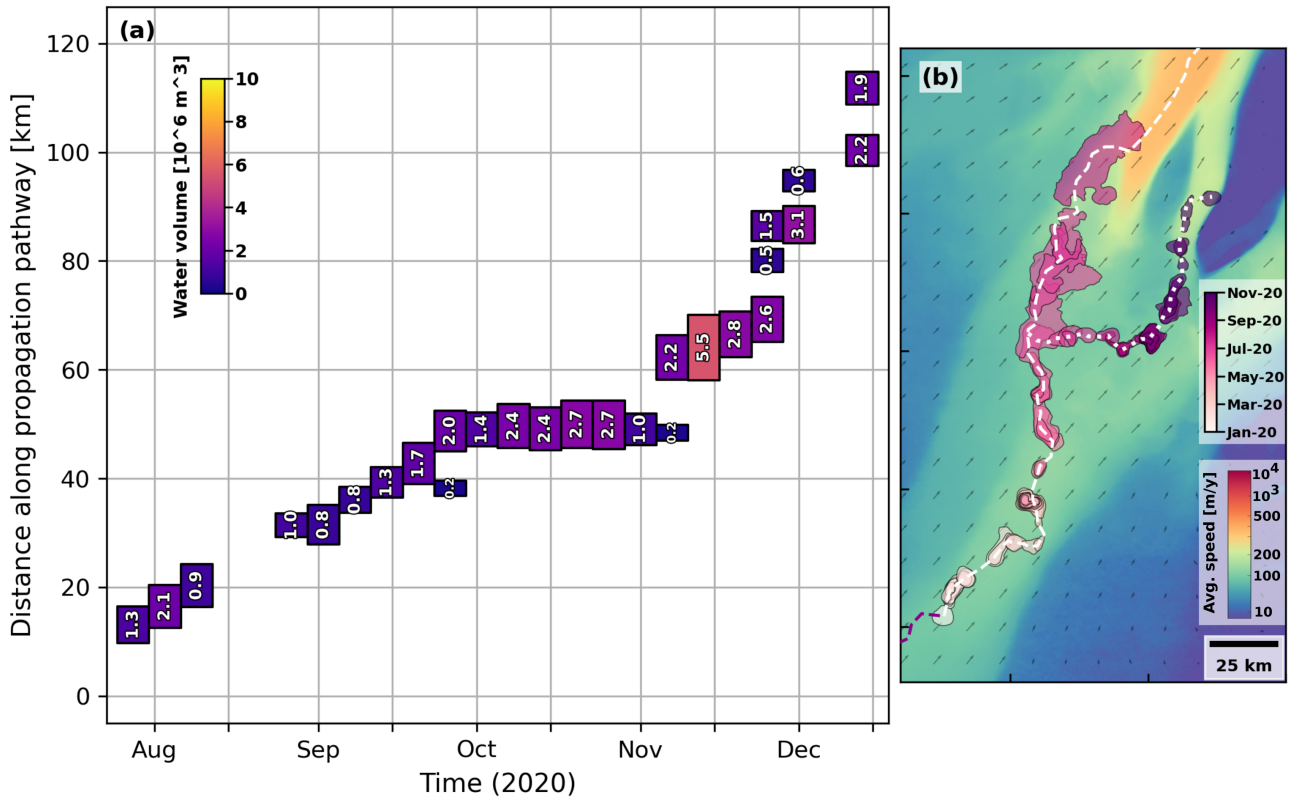

Figure S4. Same as Figure 3 in the main text, but instead showing an overview of the secondary branch of the propagation pathway, indicated by the white dotted line in (b).

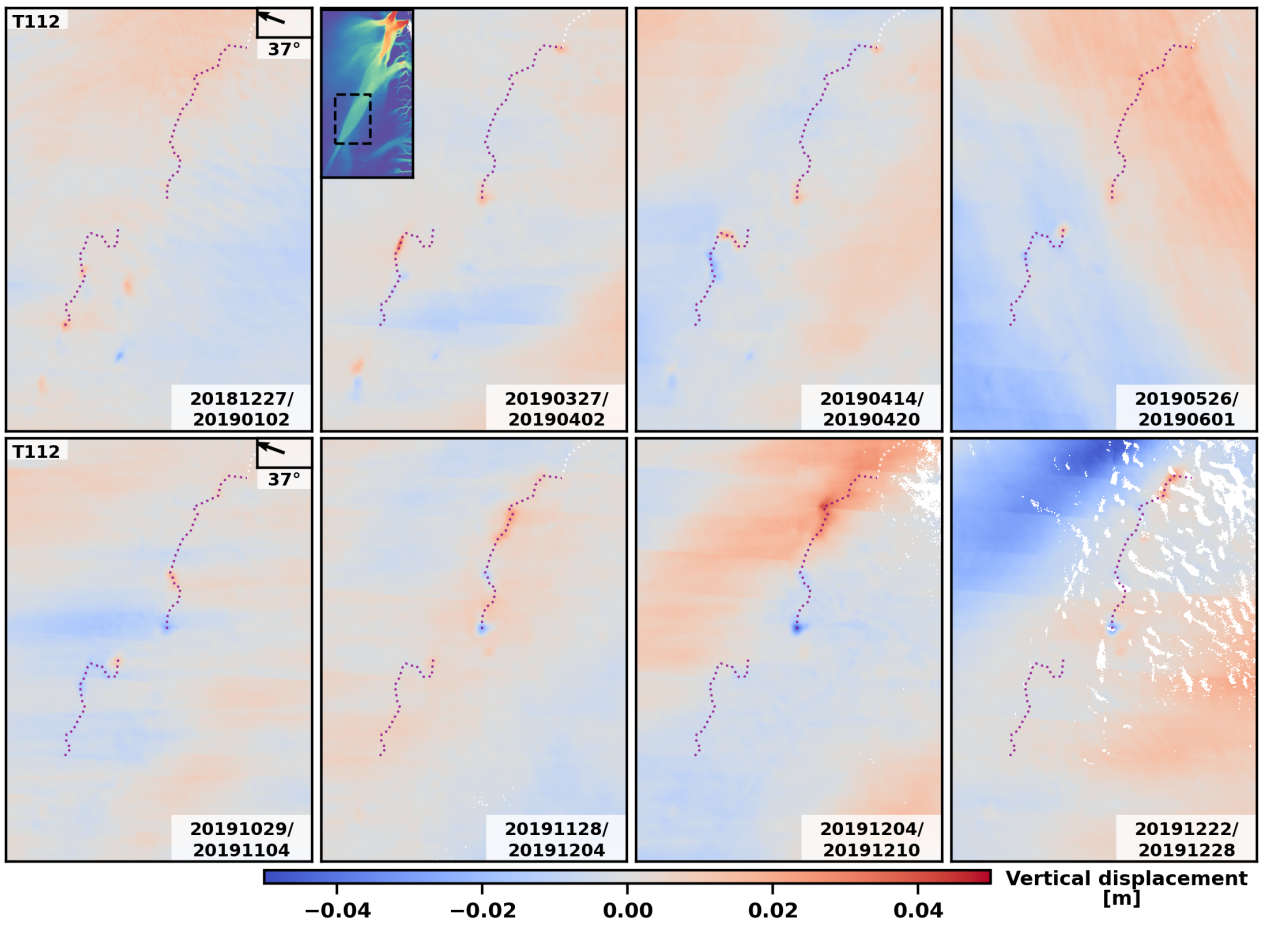

Figure S5. Vertical displacement anomaly maps, inferred from Sentinel-1 DInSAR LoS velocity anomaly measurements from track 112, covering the far upstream NEGIS region for 6-day periods during December 2018 to December 2019. The purple and white lines indicate the observed propagation pathways (same as in Figure 1). Note that uplift and subsidence magnitudes are substantially lower than those observed in further downstream regions.

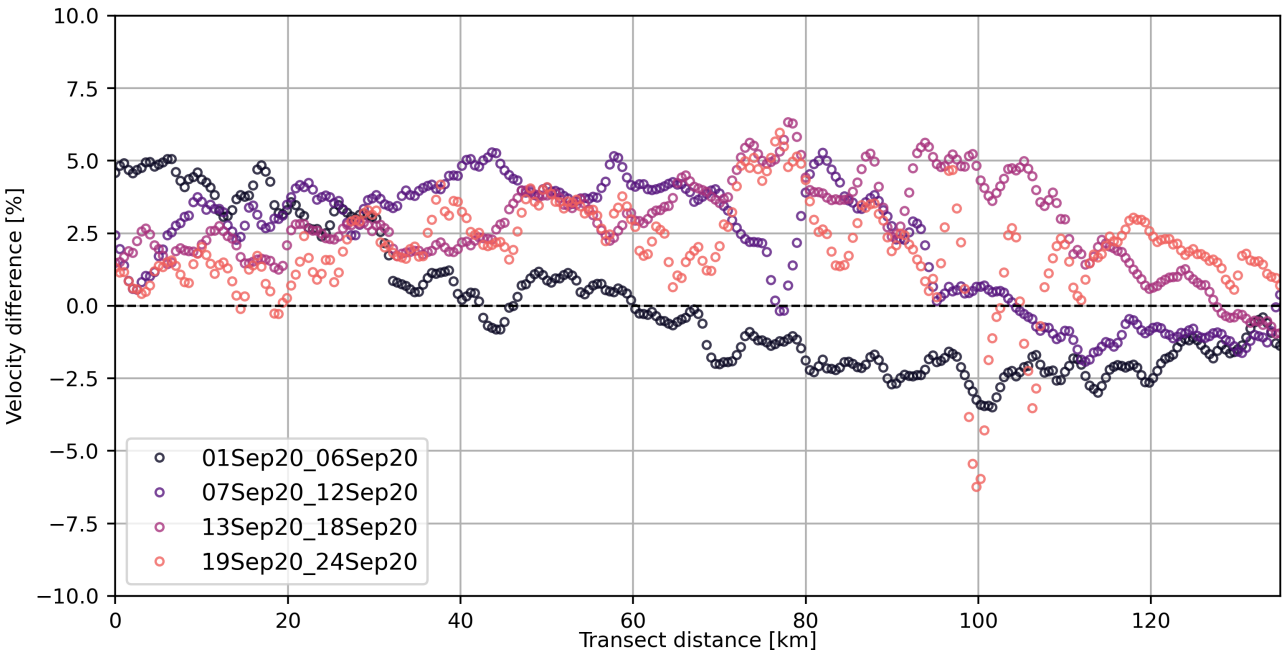

Figure S6. Relative difference in velocity magnitude from MEaSUREs 2020 horizontal velocity mosaics with respect to October-November average along the transect shown in Figure 4 in the main text (black dashed line). Note the "wave" pattern in the data, where maximum velocity is observed in early September in the upstream parts of the transect and late September in the downstream parts, matching the timing of the propagating drainage cascade observed with DInSAR (see Figure 2 in the main text).

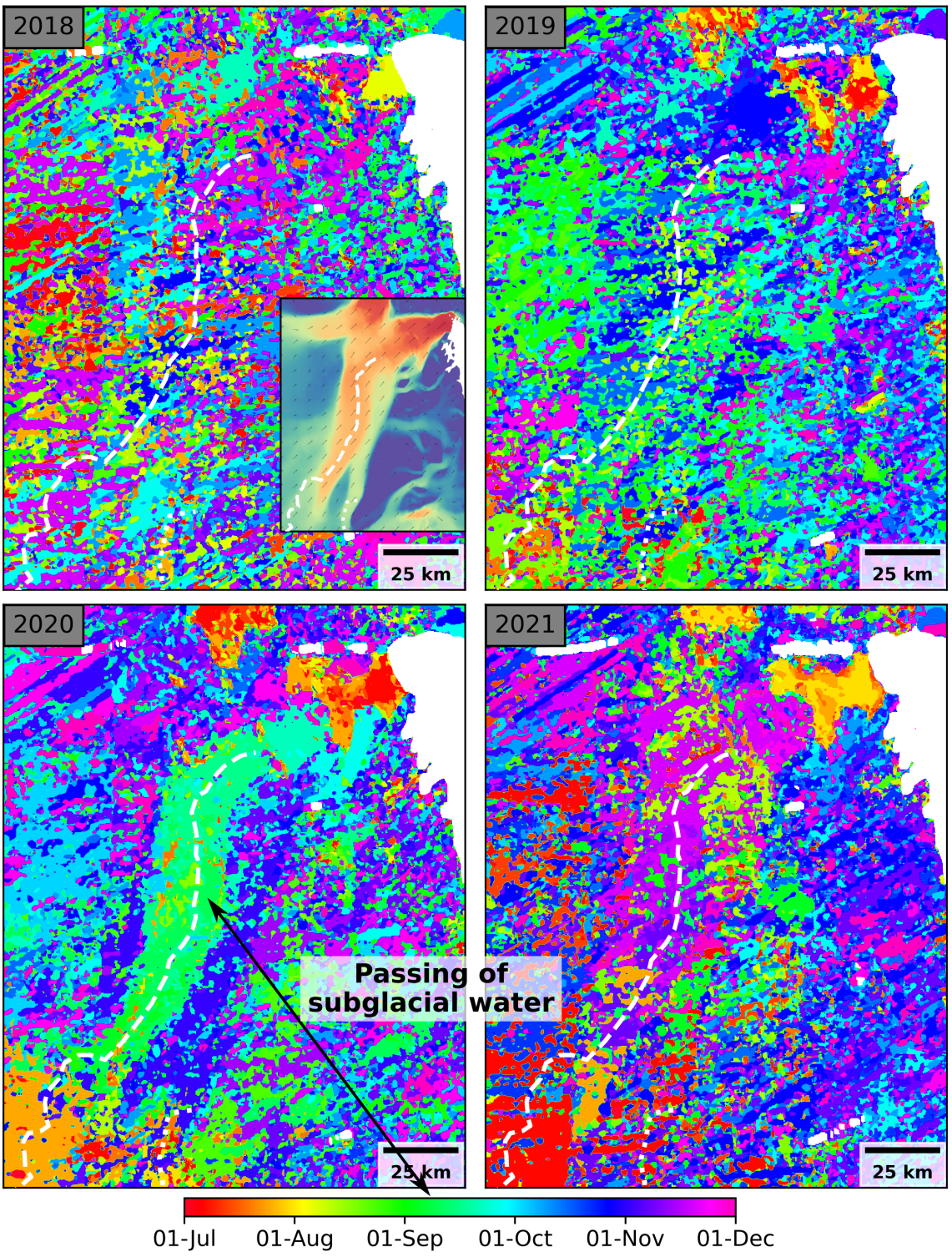

Figure S7. (Caption on next page).

Figure S7. (Previous page) Time of peak velocity magnitude between July 1st and December 1st from NASA MEaSUREs 6-day 2D Sentinel-1 velocity mosaics, shown in the downstream ZI region (inset map top left panel). Individual velocity mosaics have been spatially averaged with an 8x8 window. The dashed white line indicates (in all panels) the propagation pathway of the observed 2020 uplift events. In years 2018 and 2019, when no subglacial drainage events were detected, the peak time appears relatively random, however in 2020, a majority of the downstream ZI region shows peak velocity during September, coincident with the observed drainage event. For 2021, the measurements are slightly less clear, however several downstream areas experience peak velocity in late November, coincident with the 2021 drainage event.

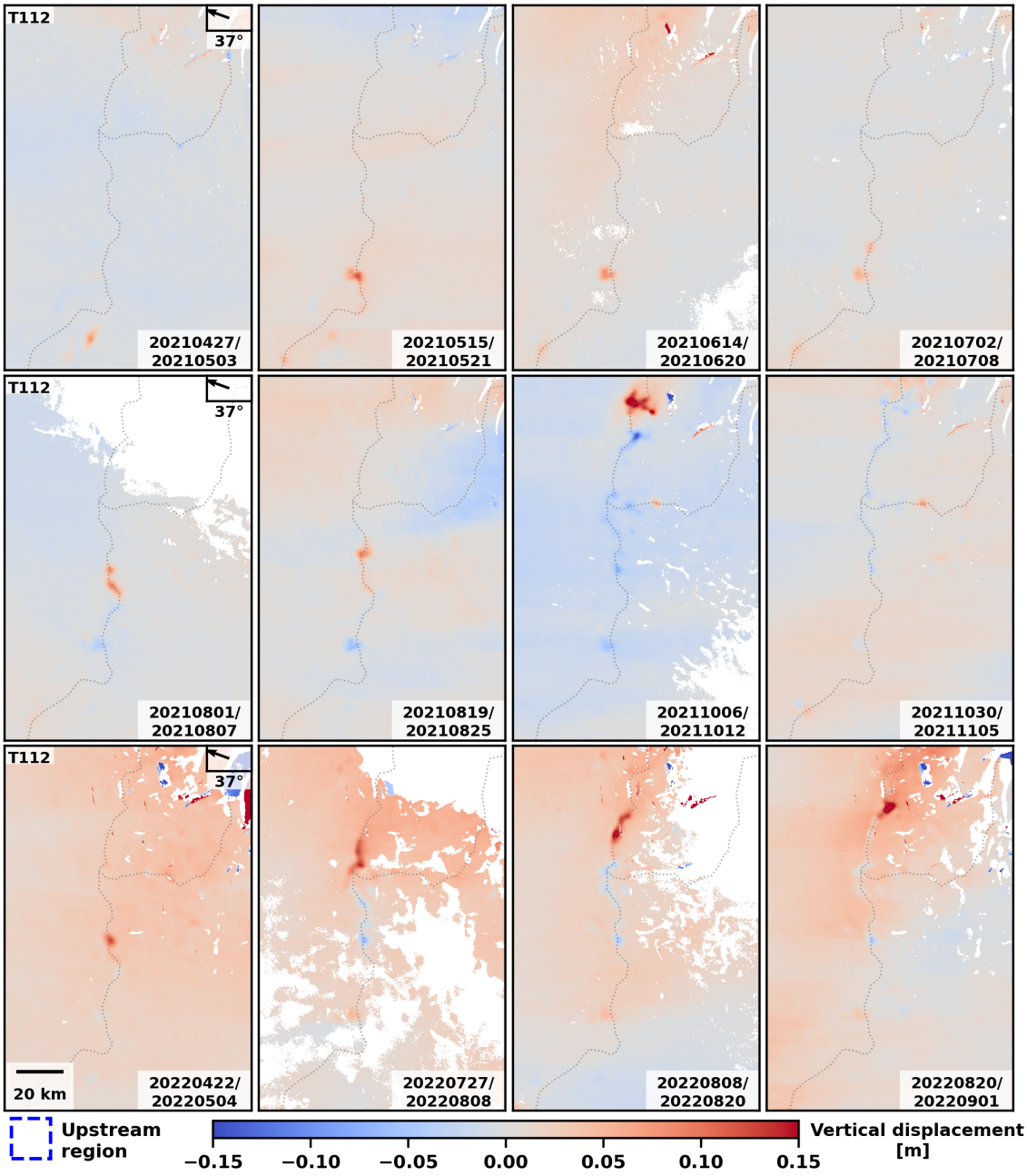

Figure S8. Vertical displacement anomaly maps, inferred from Sentinel-1 DInSAR LoS velocity anomaly measurements from track 112, covering the upstream NEGIS region (blue rectangle in Figure 1) for 6-day periods during the period April 2021 to August 2022. The gray lines indicate the propagation pathway observed for the 2020 drainage cascade (Figs. 1-3).

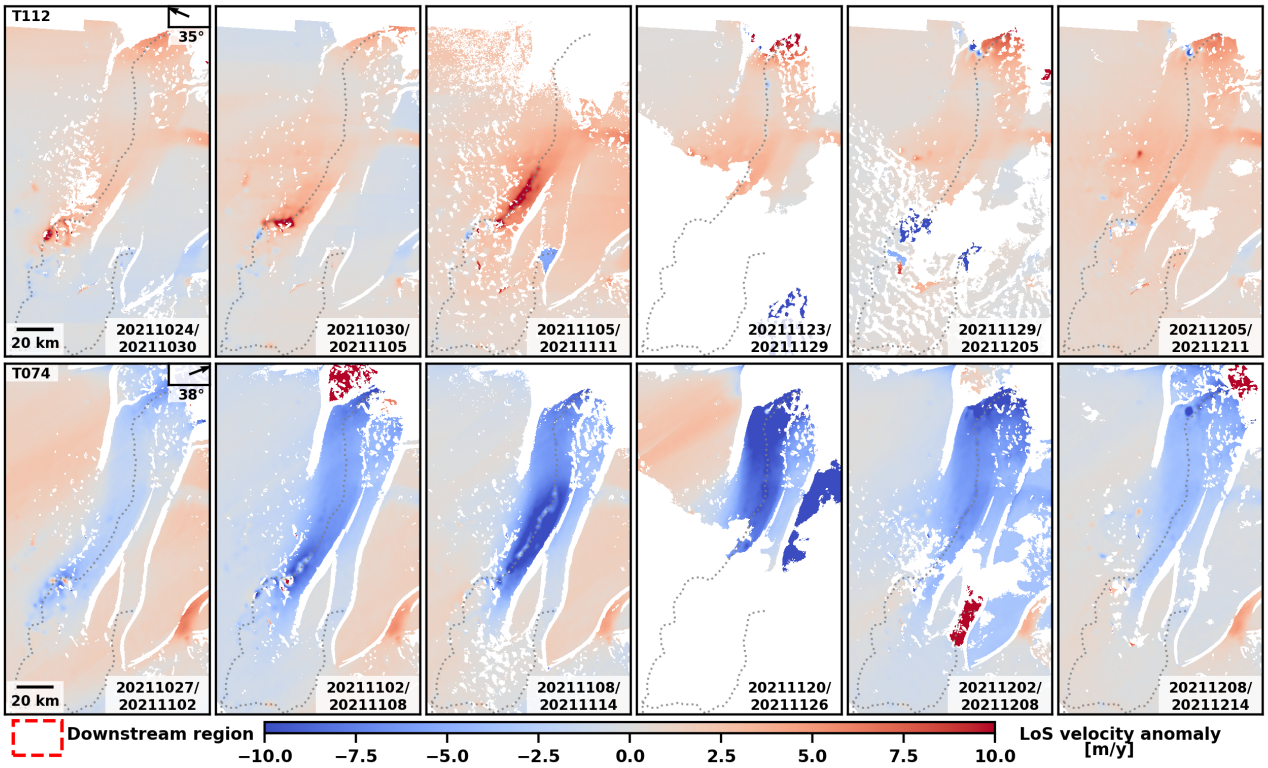

Figure S9. DInSAR LoS velocity anomaly maps from Sentinel-1 tracks 112 (top row) and 74 (bottom row) covering the downstream NEGIS region (red rectangle in main text Figure 1), documenting the drainage events observed in October/November 2021. The top right corner of each column's first panel shows the ground-projected LoS direction and incidence angle for the given row. The dashed/dotted lines outline the propagation pathways followed by the uplift events observed in 2020 (same as main text Figure 1). Similarly to the 2020 case, the DInSAR measurements suggest both local uplift/subsidence patterns as well as a spatially broader increase in flow speed. Note that the uplift "bead-and-thread" structure of these events closely follows the drainage pathway inferred from the 2020 data.